Physics of Fluids

RESEARCH ARTICLE | APRIL 05 2023

Helical model based on artificial neural network for large eddy simulation of compressible wall-bounded turbulent flows

Liu Wanhai (刘万海) ; Qi Han (齐涵) ; Shi Haoyu (史颢宇) ; Yu Changping (于长平) ;
Li Xinliang (李新亮)

Physics of Fluids 35, 045120 (2023)
https://doi.org/10.1063/5.0137607

Physics of Fluids ARTICLE scitation.org/journal/phf

Helical model based on artificial neural network for large eddy simulation of compressible wall-bounded turbulent flows

Cite as: Phys. Fluids **35**, 045120 (2023); doi: 10.1063/5.0137607
Submitted: 4 December 2022 · Accepted: 4 February 2023 ·
Published Online: 5 April 2023

Wanhai Liu (刘万海),[1,2] Han Qi (齐涵),[2] Haoyu Shi (史颢宇),[3] Changping Yu (于长平),[2,a)] and Xinliang Li (李新亮)[2]

AFFILIATIONS

[1]Intelligent Manufacturing of Zhejiang Guangsha Vocational and Technical University of Construction, Dongyang 322100, China
[2]LHD, Institute of Mechanics, Chinese Academy of Sciences, Beijing 100190, China
[3]Department of Mechanics, Lanzhou University, Lanzhou 730000, China

[a)]Author to whom correspondence should be addressed: cpyu@imech.ac.cn

ABSTRACT

Similar to the kinetic energy cascade, a helicity cascade is also a basic and key process in the generation and evolution of the turbulent flows. Furthermore, the helicity flux (HF) plays a crucial role between two scales in the helicity cascade. In this study, we will supply a new helical model constrained by the helicity flux for the large eddy simulation of the compressible turbulent flows. Then, in order to obtain a more precise HF, the local coefficient of the modeled HF is determined by the artificial neural network (ANN) method. The new model combines merits of the high robustness and the correlation with the real turbulence. In the test case of the compressible turbulent channel flow, the new model can supply a more accurate mean velocity profile, turbulence intensities, Reynolds stress, etc. Then, for the test in the compressible flat-plate boundary layer, the new model can also precisely predict the onset and peak of the transition process, the skin-friction coefficient, the mean velocity in the turbulent region, etc. Moreover, the ANN here is a semi-implicit method, and the new model would be easier to be generalized to simulate other types of the compressible wall-bounded turbulent flows.

I. INTRODUCTION

In three-dimensional (3D) turbulent flows, the helicity $h = \boldsymbol{u} \cdot \boldsymbol{\omega}$, the scalar product of the velocity $\boldsymbol{u}$ and the corresponding vorticity $\boldsymbol{\omega}$, is the sole chiral quadratic inviscid invariant.[1] The helicity plays the central role in many natural phenomena and engineering flows, such as hurricanes, tornadoes, Langmuir circulations in the oceans, and rotating machinery.[2–4]

In 3D turbulence, both the energy and the helicity are inviscid invariants, indicating that the helicity may also cascade to small scales just as the energy cascade.[5] However, different from the energy, the helicity is a topological invariant, which can measure the knottedness, or amount of the linkage of vortex lines.[6] In 3D turbulence, the helicity may be negative, showing different dynamics and cascades.[7] Brissaud *et al.* proposed two types of cascades showing the pure helicity cascade and the joint cascades of the energy and the helicity.[8] However, Kraichnan deemed that the first possibility is not reasonable but the second is more plausible.[9] Then, the joint cascade of energy and helicity is revealed from the properties of Euler equations.[8,10] This picture of cascades in the helical turbulence was subsequently tested and verified through the Gledzer–Ohkitani–Yamada shell model for the turbulence.[11,12] In the joint cascade process of the energy and the helicity, the helicity flux (HF) has more intermittent than the energy one.[13] Using a phenomenological approach, a distortion timescale (τ_H) for the helicity cascade can be deduced, and it is in analogy to that for the energy cascade (τ_E).[14] The value of the ratio τ_E/τ_H can be measured by the square root of the spectral relative helicity $\{\alpha(k) = |H(k)|/[2kE(k)]$ [$H(k)$ and $E(k)$ are the helicity and energy spectra, respectively]$\}$, and $\alpha(k) \sim 1/k$ for the parallel cascade regime. The mean spectral relative helicity showed the scale as $k - 1$ in the inertial range from the simulation result.[15,16]

As a prospective technique, large-eddy simulation (LES) has been widely used in the simulation of the turbulent flows for different fields, including the science research and engineering. Due to the high robustness, the eddy-viscosity model is the most popular LES model, and the Smagorinsky model (SM) is the first one proposed by Smagorinsky and Deaedorff.[17,18] Later, several different models were

suggested. The wall-adapting local eddy-viscosity model (WALE) was suggested by Nicoud and Ducros,[19] and it can simulate correct asymptotic behavior in the near-wall region. Vreman proposed the Vreman model[20] and it is a low dissipation eddy-viscosity model which can also predict transitional flow well. Considering the helicity effects in the helical turbulence, Yu *et al.* first introduced the helicity flux to construct a new eddy-viscosity model,[21] which can improve the simulation result apparently. Then, the helical model (HM) was rectified and applied to simulate the compressible transitional flows.[22] The merit of the eddy-viscosity model is robustness, and its shortcoming is low correlation with the real turbulence. Also, there still are other types of LES models. The scale-similarity model is one of the structural models proposed by Bardina, Ferziger, and Reynolds, and it needs a second filtering.[23] The gradient model is another structural model deduced from Taylor expansions for subgrid-scale stress (SGS).[24] Different from the eddy-viscosity model, the structural model has the merits of high correlation with the real turbulence but the shortcoming is low robustness.

Recently, artificial neural networks (ANNs) are playing an important role in turbulence modeling. Ling *et al.* proposed a new multiplicative-layer neural network to predict the Reynolds stress anisotropic tensor for the first time.[25] Using machine learning and through optimal evaluation theory analysis, Vollant *et al.* obtained a new SGS scalar flux model,[26] which can predict results much closer to the direct numerical simulation (DNS) results. Using the ANN method, Xie *et al.* suggested the coefficients of the mixed SGS model for LES of the compressible isotropic turbulence and the new model can supply a better result than the traditional LES model.[27] Zhou *et al.* proposed a new SGS model based on the ANN method for the isotropic turbulence,[28] and the dependence of the SGS model on the filter width was considered. Based on the ANN method, a series of nonlinear algebraic models and deconvolutional models were developed recently,[29–31] and they could improve the accuracy of the model clearly. Park and Choi suggested a new method for modeling the SGS model which could show good performance and was not affected by the grid resolution.[32] Many SGS models based on ANN method are established for the isotropic turbulence and few of them are proposed for more complex flows, such as the transition flow, the separated flow and the flow with complex-geometry boundaries. In addition, low efficiency is still a problem for ANN method on turbulence modeling, and it need to be improved. On the other hand, we have known that ANN method can improve the predicting precision, and it has been well applied to recognize the elaborate turbulent structures, and also it is a better tool to model high-precision turbulence model.

In this study, we propose a new helical model (NHM) based on the ANN method for the LES of the compressible flow. In this new model, the existing helical model[21,22] is constrained by the helicity flux. To obtain the correct coefficient of the helicity flux, the ANN method is introduced for LES modeling. In this paper, the governing equations and the LES models are illustrated in Sec. II. The new helical model is deduced in Sec. III. In Sec. IV, the new model is tested and compared with others. Finally, we supply the conclusions in Sec. V.

II. GOVERNING EQUATIONS AND SGS MODELS

The derivation of the filtered N–S equations for the LES of the compressible turbulence is as follows:

$$\frac{\partial \bar{\rho}}{\partial t}+\frac{\partial \bar{\rho}\widetilde{u}_j}{\partial x_j}=0, \tag{1}$$

$$\frac{\partial \bar{\rho}\widetilde{u}_i}{\partial t}+\frac{\partial \bar{\rho}\widetilde{u}_i\widetilde{u}_j}{\partial x_j}=-\frac{\partial \bar{p}}{\partial x_i}+\frac{\partial \widetilde{\sigma}_{ij}}{\partial x_j}-\frac{\partial \tau_{ij}}{\partial x_j}, \tag{2}$$

$$\frac{\partial \bar{\rho}\widetilde{E}}{\partial t}+\frac{\partial (\bar{\rho}\widetilde{E}+\bar{p})\widetilde{u}_j}{\partial x_j}=-\frac{\partial \widetilde{q}_j}{\partial x_j}+\frac{\partial \widetilde{\sigma}_{ij}\widetilde{u}_i}{\partial x_j}-\frac{\partial C_pQ_j}{\partial x_j}-\frac{\partial J_j}{\partial x_j}, \tag{3}$$

and supplemented by the filtered state equation as follows:

$$\bar{p}=\bar{\rho}R\widetilde{T}. \tag{4}$$

Here, $(\bar{\cdot})$ represents spatial filtering with a low-pass filter at scale Δ and $(\widetilde{\cdot})$ represents the Favre filtering ($\widetilde{\phi}=\overline{\rho\phi}/\bar{\rho}$). $\bar{\rho}$, $\widetilde{u}_i$, $\widetilde{T}$, $\bar{p}$, and R are the filtered density, the velocity, the temperature, the pressure, and the specific gas constant, respectively.

In the equations,

$$\bar{\rho}\widetilde{E}=\bar{\rho}C_v\widetilde{T}+\frac{1}{2}\bar{\rho}\widetilde{u}_i\widetilde{u}_i \tag{5}$$

is the resolved total energy, where C_v is the specific heat at the constant volume,

$$\widetilde{\sigma}_{ij}=2\mu(\widetilde{T})\left(\widetilde{S}_{ij}-\frac{1}{3}\delta_{ij}\widetilde{S}_{kk}\right),\quad \widetilde{S}_{ij}=\frac{1}{2}\left(\frac{\partial \widetilde{u}_i}{\partial x_j}+\frac{\partial \widetilde{u}_j}{\partial x_i}\right) \tag{6}$$

is the resolved viscous stress tensor, and

$$\widetilde{q}_j=\frac{C_p\mu(\widetilde{T})}{P_r}\frac{\partial \widetilde{T}}{\partial x_j} \tag{7}$$

is the resolved heat flux vector, in which C_p is the specific heat at the constant pressure, P_r is the molecular Prandtl number, and

$$\mu=\frac{1}{Re}\left(\frac{\widetilde{T}}{\widetilde{T}_\infty}\right)^{3/2}\frac{\widetilde{T}_\infty+T_s}{\widetilde{T}+T_s} \tag{8}$$

is the dimensionless molecular viscosity calculated using Sutherland's law for given $T_s=110.3K$.

In Eqs. (2) and (3), there are still some unclosed terms, which are the SGS stress

$$\tau_{ij}=\bar{\rho}(\widetilde{u_iu_j}-\widetilde{u}_i\widetilde{u}_j), \tag{9}$$

the SGS heat flux

$$Q_j=\bar{\rho}(\widetilde{u_jT}-\widetilde{u}_j\widetilde{T}), \tag{10}$$

and the SGS turbulent diffusion term

$$J_j=\frac{1}{2}\bar{\rho}(\widetilde{u_iu_iu_j}-\widetilde{u_iu_i}\widetilde{u}_j). \tag{11}$$

The SGS turbulent diffusion can be approximated as $J_j=\tau_{ij}\widetilde{u}_i$.[33]

III. DERIVATION OF THE NEW HELICAL MODEL (NHM)

A. Proposition of the helicity flux constrained helical model

In the compressible LES equations, the eddy-viscosity model of SGS stress can be written as follows:

$$\tau_{ij}^{mod} - \frac{1}{3}\delta_{ij}\tau_{kk}^{mod} = -2\mu_{sgs}\left(\widetilde{S}_{ij} - \frac{1}{3}\delta_{ij}\widetilde{S}_{kk}\right), \tag{12}$$

where τ_{kk}^{mod} is the isotropic part of the SGS stress model and μ_{sgs} is the SGS eddy viscosity.

The eddy diffusion model of SGS heat flux is as follows:

$$Q_j^{mod} = -\frac{\mu_{sgs}}{Pr_{sgs}}\frac{\partial\widetilde{T}}{\partial x_j}. \tag{13}$$

For the helical model,[21,22] the form of the SGS stress model is as follows:

$$\tau_{ij}^{H} = -2\bar{\rho}C_r\Delta^{5/2}\widetilde{S}_{sr}\left(\widetilde{S}_{ij} - \frac{1}{3}\delta_{ij}\widetilde{S}_{kk}\right) + \frac{2}{3}C_I\bar{\rho}\Delta^3\widetilde{S}_{sr}^2\delta_{ij}, \tag{14}$$

where $\widetilde{S}_{sr} = |2\widetilde{S}_{ij}\widetilde{R}_{ij}|$ with $\widetilde{R}_{ij} = \frac{1}{2}\left(\frac{\partial\widetilde{\omega}_i}{\partial x_j} + \frac{\partial\widetilde{\omega}_j}{\partial x_i}\right)$.

The modeled SGS heat flux is

$$Q_j^{H} = -\frac{C_r\bar{\rho}\Delta^{5/2}\widetilde{S}_{sr}}{Pr_{sgs}}\frac{\partial\widetilde{T}}{\partial x_j}. \tag{15}$$

Then, the infinite series expansion[34] is introduced here as follows:

$$\overline{fg} - \bar{f}\bar{g} = \alpha\frac{\partial\bar{f}}{\partial x_k}\frac{\partial\bar{g}}{\partial x_k} + \frac{1}{2!}(\alpha)^2\frac{\partial^2\bar{f}}{\partial x_k\partial x_l}\frac{\partial^2\bar{g}}{\partial x_k\partial x_l} + \frac{1}{3!}(\alpha)^3\frac{\partial^3\bar{f}}{\partial x_k\partial x_l\partial x_m}\frac{\partial^3\bar{g}}{\partial x_k\partial x_l\partial x_m} + \cdots, \tag{16}$$

where

$$\alpha(y) = \int_{-\infty}^{\infty} 2x^2G(x,y)dx. \tag{17}$$

$G(x, y)$ in Eq. (17) is the kernel of the filter and can be designated as the box filter.

Applying the infinite series expansion to SGS stress, we can obtain

$$\tau_{ij} = \bar{\rho}(\widetilde{u_iu_j} - \widetilde{u}_i\widetilde{u}_j) = C_k\Delta_k^2\bar{\rho}\frac{\partial\widetilde{u}_i}{\partial x_k}\frac{\partial\widetilde{u}_j}{\partial x_k} + \frac{1}{2!}(C_k^2\Delta_k^2\Delta_l^2)\bar{\rho}\frac{\partial^2\widetilde{u}_i}{\partial x_k\partial x_l}\frac{\partial^2\widetilde{u}_j}{\partial x_k\partial x_l} + \cdots, \tag{18}$$

where C_k is the coefficient and Δ_k is the grid width in the x_k direction.

For simplicity, we only reserve the first term and it can be expressed as follows:

$$\tau_{ij}^{s} \approx C_k\Delta_k^2\bar{\rho}\frac{\partial\widetilde{u}_i}{\partial x_k}\frac{\partial\widetilde{u}_j}{\partial x_k}, \tag{19}$$

which is just the same form as the gradient model.[24]

The turbulent cascade has always been the core content of turbulence research,[35] since the concept of the turbulent cascade was proposed by Richardson for the first time. As mentioned above,[7,8] the helicity cascade also exists in 3D turbulence. As we know, the energy flux is the core physical quantity in the energy cascade.[36] Similar to the energy flux, the helicity flux is also the core physical quantity in the helicity cascade, and it also can reflect the cascade process. In addition, the helicity flux could be also a measurement of the turbulent structures,[6] which is also an important character for the reflection of the turbulence. Helicity flux is proportional to the product of the SGS stress tensor and the resolved vorticity gradient tensor, written as follows:[21]

$$\Pi_\Delta^H = -2\tau_{ij}\widetilde{R}_{ij}. \tag{20}$$

To get the more accurate helicity flux, we assume a ratio η_Δ existing between the real helicity flux and the simplified helicity flux, and it is a dimensionless parameter. Then, we can obtain

$$\Pi_\Delta^H = -2\eta_\Delta\tau_{ij}^s\widetilde{R}_{ij}. \tag{21}$$

Now, to make the helical model to simulate the accurate helicity flux, we use the helicity flux obtained from Eq. (21) to constrain the helicity flux from the helical model as follows:

$$-2\tau_{ij}^H\widetilde{R}_{ij} = -2\eta_\Delta\tau_{ij}^s\widetilde{R}_{ij} \tag{22}$$

and

$$\tau_{ij}^H\widetilde{R}_{ij} = \eta_\Delta\tau_{ij}^s\widetilde{R}_{ij}. \tag{23}$$

Using the constraint of Eq. (23), we can get new coefficients C_r and C_I in Eq. (14). Therefore, the NHM is obtained. However, η_Δ is still unknown.

For obtaining the coefficient η_Δ, we will introduce the artificial neural network (ANN) method in the next part.

B. Artificial neural network

In this work, we will use the ANN to confirm the relation between the input parameters and η_Δ in the compressible turbulent channel flow. The data for training and testing in this paper are obtained from the DNS data of a temporally compressible isothermal-wall turbulent channel flow. The Mach number $Ma = 1.5$ and the Reynolds number $Re = 3000$. The main characteristics of the DNS of the channel flow are listed in Table I. In the process of training and testing, the DNS data are filtered in the streamwise and the spanwise directions with a top-hat filter.

In Fig. 1, we show the schematic diagram of the ANN. The ANN is composed of multiple layers with many neurons. The neurons receive the input signals from the previous layer and send them to the next layer by the successive mathematical operation of the linear weighted sum and nonlinear activation. In the lth layer, each neuron receives the inputs $X_i^{(l-1)}$ from $(l-1)$ layer and then transmits them to the outputs $X_i^{(l)}$ activated by the nonlinear function. The transfer function from the $(l-1)$th layer to the lth one is calculated as follows:

$$X_i^{(l)} = \sigma\left[b_i^{(l)} + \sum_j W_{ij}^{(l)}X_j^{(l-1)}\right], \tag{24}$$

TABLE I. Main characteristics of the DNS data for training and testing.

	Computation domain	Grids	Δx^+	Δy_w^+	Δz^+	Re_τ
DNS	$4\pi \times 2 \times 4/3\pi$	$900 \times 201 \times 300$	2.99	0.32	2.99	220

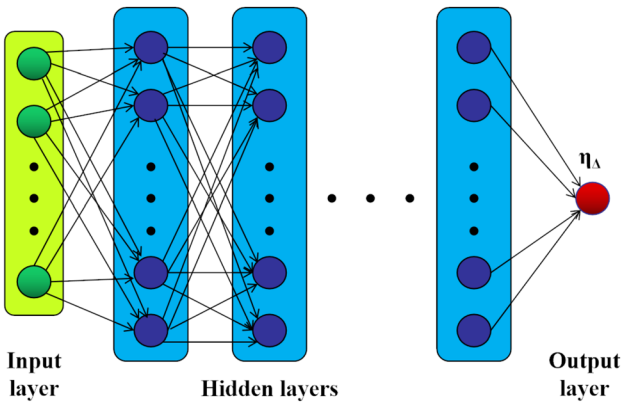

FIG. 1. Schematic diagram of the ANN for predicting η_Δ.

where $\sigma[\cdot]$ is the nonlinear activation function and $W_{ij}^{(l)}$ and $b_i^{(l)}$ are the weights and biases in the lth layer, respectively.

The input parameters of the ANN are critical for predicting η_Δ. The variables are dimensionless quantities, where several variables may be selected in compressible wall-bounded turbulence, such as Δ^+, y^+, Re_Δ, and Δ_l^+. In this paper, $\Delta^+ = \bar{\rho}_w \widetilde{u}_\tau \Delta/\mu_w$ is the normalized filter width, $y^+ = \bar{\rho}_w \widetilde{u}_\tau y/\mu_w$ is the dimensionless normal distance, $Re_\Delta = \rho_w |\widetilde{S}| \Delta^2/\mu_w$ is the mesh Reynolds number, and $\Delta_l^+ = \Delta/l$ with $l = [\mu_w^2/(2\bar{\rho}_w \langle \widetilde{S}_{ij} \widetilde{S}_{ij} \rangle)]^{1/4}$. Here, $\widetilde{u}_\tau = \sqrt{\tau_w/\bar{\rho}_w}$ is the filtered wall friction velocity with $\tau_w = \mu_w \frac{\widetilde{\partial u}}{\partial y}$ being the wall shear stress and $\langle \cdot \rangle$ denoted as the spatial average along the homogeneous directions. Additionally, we also supply the respective helicity $\alpha(\Delta) = |\Delta H(\Delta)|/[2\Delta E(\Delta)]$ for predicting the ratio of helicity flux. A total of four layers (one input layer, two hidden layers, and one output layer) with neurons in the ratio $M : 100 : 100 : 1$ are supplied in this study, and M is the number of input variables which is listed in Table II. The hyperbolic tangent function $[\sigma_h(x) = (e^x - e^{-x})/(e^x + e^{-x})]$ and linear function $[\sigma_o(x) = x]$ are the activation ones of the hidden layers and output layer. The mean-squared error (MSE) function is chosen as the loss function of the ANN, and it can be defined as

TABLE II. A set of inputs and outputs for different ANN models.

Model	ANN1	ANN2	ANN3
Inputs	$\Delta^+, y^+, \alpha(\Delta)$	$\Delta_l^+, y^+, \alpha(\Delta)$	$Re_\Delta, y^+, \alpha(\Delta)$
Outputs	η_Δ	η_Δ	η_Δ

$L = \langle (\eta_\Delta^{true} - \eta_\Delta^{pred})^2 \rangle$, where η_Δ^{true} and η_Δ^{pred} denote the true and predicted values of the ANN.

In this paper, 2×10^4 samples are chosen from 20 snapshots of the filtered DNS data with a ratio of the filter width Δ/Δ_{DNS} ranging from 2 to 20. Then, using the cross-validation strategy, we divide the dataset into a training set and a testing set to hold down parameter overfitting of the ANN; 70% of the samples are randomly selected from the total dataset as the training set, while the others as the testing set. The weights of the ANN are initialized by the Glorot-uniform algorithm and optimized by the Adam algorithm[37] for 1×10^4 iterations, with a batch size and learning rate of 1000 and 0.01, respectively. In addition, to obtain the optimal hyperparameters including the numbers of layers and neurons and the types of activation functions, the grid search method is selected as the hyperparameter pruning method of the ANN. In Fig. 2, we show the learning curves of the different ANN models. After a period of training with 1×10^4 epochs, the MSE losses in both the training and the testing sets converge quickly and reach the stationarity. The training and the testing losses for all the models are close, which means that the chosen hyperparameters are reasonable and all the ANN models are well trained. At the same time, we can also see that the ANN3 has the smallest loss among the three ANN models.

Through calculating three metrics to measure the difference between the true value η_Δ^{true} from the filtered DNS data and the predicted value η_Δ^{model} obtained from the ANN, we can well evaluate the performance of different ANN models. The three metrics are the correlation coefficient $C(\eta_\Delta)$, the relative error $E_r(\eta_\Delta)$ and the ratio of the root mean square value $R(\eta_\Delta)$, which are expressed, respectively, as follows:

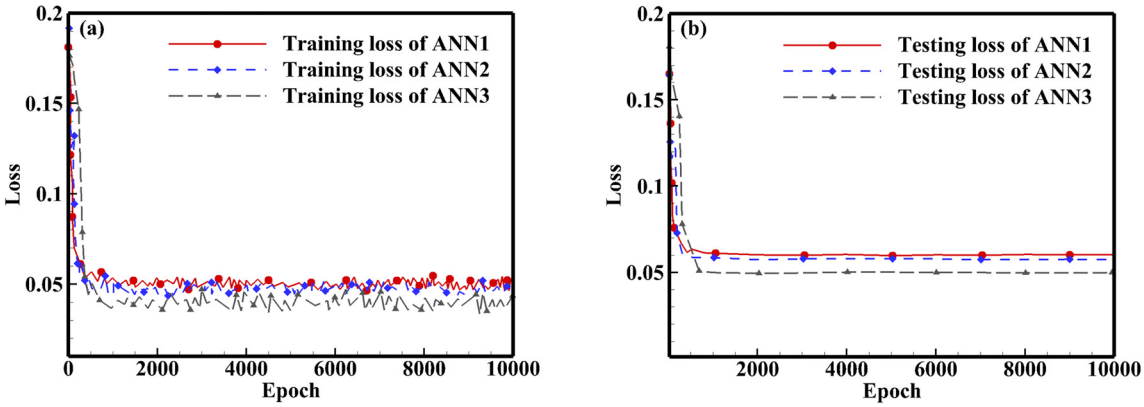

FIG. 2. Learning curves of the proposed ANN models for predicting the coefficient η_Δ: (a) training loss for ANN models and (b) testing loss for ANN models.

TABLE III. Correlation coefficient (C), relative error (E_r), and ratio of root mean square value (R) of the coefficient η_Δ in different datasets for different ANN models.

Dataset/C(η_Δ)	ANN1	ANN2	ANN3
Training	0.912	0.921	0.923
Testing	0.901	0.904	0.912
Dataset/$E_r(\eta_\Delta)$	ANN1	ANN2	ANN3
Training	0.106	0.111	0.112
Testing	0.113	0.119	0.122
Dataset/R(η_Δ)	ANN1	ANN2	ANN3
Training	0.911	0.922	0.923
Testing	0.891	0.906	0.913

$$C(\eta_\Delta) = \frac{\langle (\eta_\Delta^{real} - \langle \eta_\Delta^{real} \rangle)(\eta_\Delta^{model} - \langle \eta_\Delta^{model} \rangle) \rangle}{\langle (\eta_\Delta^{real} - \langle \eta_\Delta^{real} \rangle)^2 \rangle^{1/2} \langle (\eta_\Delta^{model} - \langle \eta_\Delta^{model} \rangle)^2 \rangle^{1/2}}, \tag{25}$$

$$E_r(\eta_\Delta) = \frac{\langle (\eta_\Delta^{real} - \eta_\Delta^{model})^2 \rangle^{1/2}}{\langle (\eta_\Delta^{real})^2 \rangle^{1/2}}, \tag{26}$$

$$R(\eta_\Delta) = \frac{\langle (\eta_\Delta^{model} - \langle \eta_\Delta^{model} \rangle)^2 \rangle^{1/2}}{\langle (\eta_\Delta^{real} - \langle \eta_\Delta^{real} \rangle)^2 \rangle^{1/2}}. \tag{27}$$

In Table III, we show the comparisons of the correlation coefficients, relative errors, and ratios of root mean square values for the helicity flux ratio η_Δ in both the training and testing sets. We find that there exists slight differences between the results of the training and testing sets, and it indicates that none of the trained ANN models are overfitted. From the table, we can also see that the ANN3 model performs better than the others. The correlation coefficient and relative error of the ANN3 model in the training dataset are 92.3% and 11.2%, and 91.2% and 12.2% in the testing dataset, respectively. The ratio of the root mean square value of the ANN3 model is 92.3% and 91.3%, respectively, and they are both very close to 100%, which means that the ANN3 model can better reconstruct the helicity ratio. More importantly, all the input variables are local, which indicates that it could be easy to be generalized to other types of the compressible wall-bounded turbulence. In Fig. 3, we show the comparisons of the coefficient η_Δ reconstructed by different ANN models along the normal direction with different filter widths. From the figures, we know that the modeled helicity flux by the ANNs models has perfect agreement with the DNS results. All the factors considered, we choose the ANN3 as the

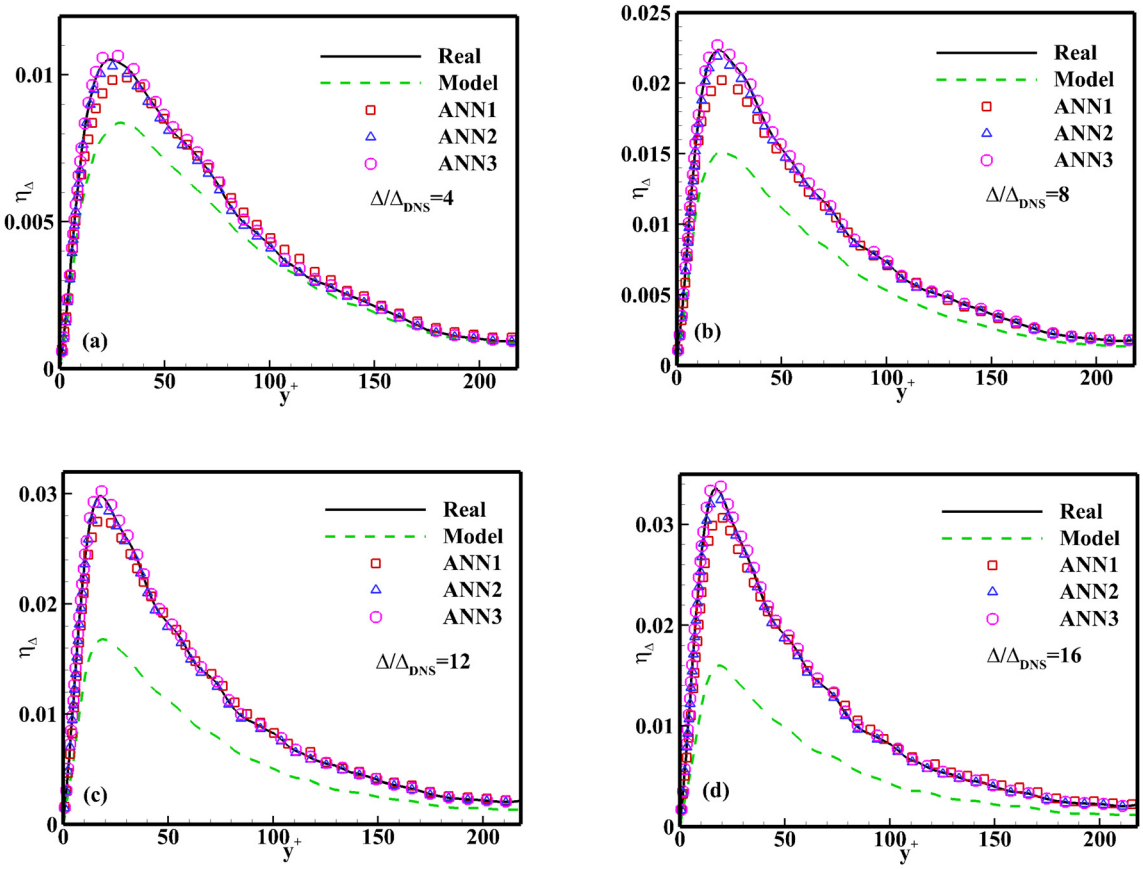

FIG. 3. Comparisons of the coefficient η_Δ reconstructed by different ANN models along the normal direction with different filter widths: (a) $\Delta/\Delta_{DNS} = 4$; (b) $\Delta/\Delta_{DNS} = 8$; (c) $\Delta/\Delta_{DNS} = 12$; and (d) $\Delta/\Delta_{DNS} = 16$.

TABLE IV. The grid setting and the main parameters for the simulations in the compressible turbulent channel flow.

	Grids	Δx^+	Δy_w^+	Δz^+	Re_τ	$-B_q$	τ_w
DNS	$900 \times 201 \times 300$	2.99	0.32	2.99	220	0.0445	0.00392
Vreman	$48 \times 65 \times 48$	56.48	1.05	18.83	207	0.0416	0.00351
WALE	$48 \times 65 \times 48$	54.86	1.02	18.28	201	0.0419	0.00368
DSM	$48 \times 65 \times 48$	57.55	1.07	19.20	210	0.0429	0.00372
HM	$48 \times 65 \times 48$	57.57	1.07	19.21	215	0.0431	0.00381
NHM	$48 \times 65 \times 48$	57.60	1.07	19.23	219	0.0443	0.00389

following testing model because it shows the best behaviors among the three ANN models. The newly constructed helicity flux ANN is a semi-explicit model, beneficial to be generalized to other type of wall-bounded turbulence. Hitherto, we finish the NHM based on the ANN method, and we will test NHM in Sec. IV.

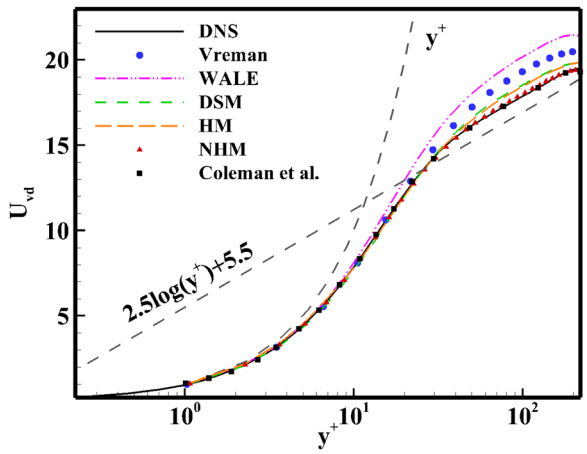

FIG. 4. The profiles of the Van Driest the transformed mean velocity normalized by u_τ from the Vreman, the WALE, the DSM and the NHM, and the DNS for comparisons. The results from Coleman *et al.*[38] are also listed here for comparison.

IV. TESTING RESULTS AND ANALYSES

A. Application in the compressible channel flow

In this section, the new model is applied in the compressible turbulent channel flow firstly. The case setting of the LES is same as that of the DNS case for ANN in Sec. III. The filtered Navier–Stokes equations are solved by a high-precision non-dimensional finite-difference solver in Cartesian coordinates: the equations are temporally integrated by the third-order Runge–Kutta scheme, and the convective and viscous terms are discretized using a sixth-order central-difference

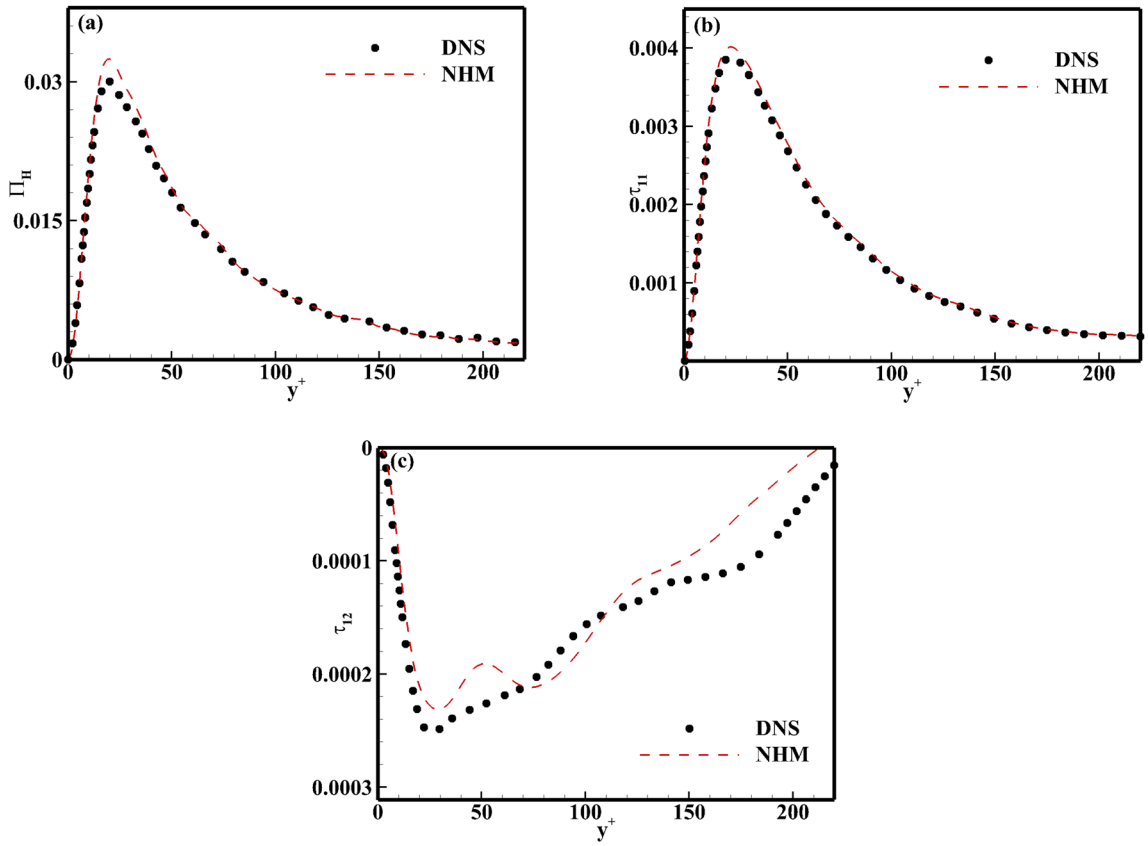

FIG. 5. Different quantities from NHM and DNS obtained *a priori*: (a) the helicity flux Π_H; (b) the component of SGS stress τ_{11}; and (c) the component of SGS stress τ_{12}.

scheme. For DNS, a seventh-order upwind difference scheme is applied to discrete the convective term, and a sixth-order central difference scheme is applied to discrete the viscous term. The grid filter width is $\Delta = (\Delta_x \Delta_y \Delta_z)^{1/3}$, where Δ_x, Δ_y, and Δ_z represent the three-direction local grid width, and the test-filter width is 2Δ for the dynamic model. Table IV shows the grid setting and the main parameters for the simulations in the compressible turbulent channel flow. For comparison, we will select three chiefly used SGS models: the Vreman, the WALE, the HM, and the dynamic Smagorinsky model (DSM).

In Fig. 4, we show the profiles of the Van Driest transformed mean velocity ($U_{vd} = \int_0^U \sqrt{\langle\rho\rangle/\rho_w} d\langle U\rangle$) obtained from models of the NHM, the Vreman, the WALE, the HM and the DSM, and DNS results are also listed here for comparisons. We can see the velocity profile from the NHM is tightly close to the DNS result, which is much better than those from other models. As expected, for $y^+ < 5$, the mean streamwise velocity generally increases linearly with y^+. In the viscous sublayer, almost all the results from the SGS models collapse to the DNS result perfectly. In the buffer layer, all the models except the WALE still show good behavior. In the log-law region, the NHM shows obvious advantage than others, and the DSM behaves better than the Vreman.

We show different quantities from the NHM and DNS obtained *a priori* in Fig. 5. From the figures, we can know that the NHM can well predict the helicity flux and the SGS stress.

Figures 6(a)–6(c) shows the profiles of the streamwise, the wall-normal, and spanwise turbulence intensities from the different models and normalized by u_τ. Totally, we can see that the result of the NHM shows better behavior than the others apparently, especially in the buffer region of the flow. In Fig. 6(d), we show the distribution of the normalized Reynolds stress R_{uv} along the normal height y^+, and the results of the DNS, the Vreman, the WALE, the HM, the DSM, and the NHM are compared together. Compared with the results of other SGS models, the NHM gives a perfect total Reynolds stress R_{uv} in almost all of the regions. The results in Fig. 5 also prove that the NHM can also supply better simulation of the high-order statistics of the turbulence.

In Fig. 7, we supply the profiles of the mean temperature $T_{av}^+ = (T_w - \langle T\rangle)/T_\tau$ ($T_\tau = B_q T_w$ is the friction temperature, $B_q = q_w/(\rho_w c_p u_\tau T_w)$ is the non-dimensional heat flux, and q_w is the wall-normal heat flux) obtained from the Vreman, the WALE, the HM, the DSM, the NHM, and the DNS. The results of all the models are not much different, but well close to the DNS result. However, after carefully identifying, we can still find that the NHM shows a little advantage over the others. In Fig. 8, the temperature fluctuations from the DNS and the selected models are compared together. Different from the mean temperature profile, the temperature fluctuation from the NHM shows much better than other results.

To further observe the performance of the NHM, we show the profiles of the resolved root mean square (rms) density fluctuations from different SGS models and DNS in Fig. 9. As the figure shows, the results from the NHM are better than those from other SGS models.

From the testing results in the compressible turbulent channel flow, we can know that the NHM has an obvious improvement in contrast to other commonly used model.

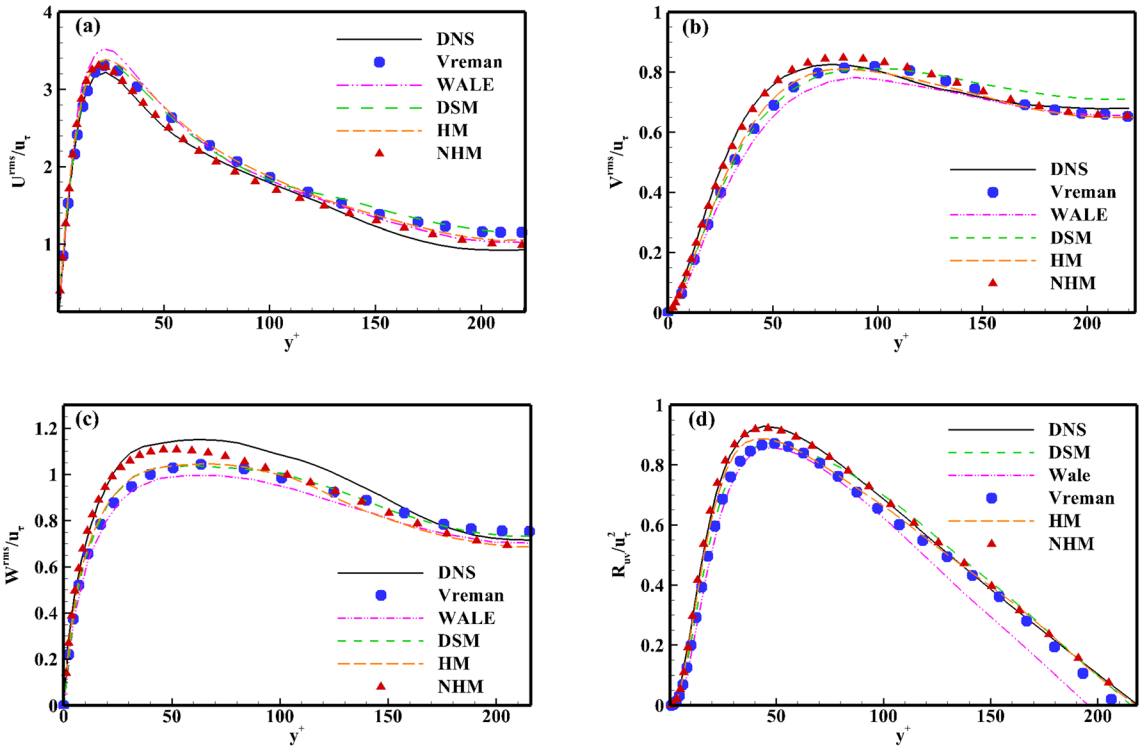

FIG. 6. Turbulence intensities and the Reynolds stress from DNS and different models: (a) streamwise turbulence intensity; (b) wall-normal turbulence intensity; (c) spanwise turbulence intensity; and (d) Reynolds stress.

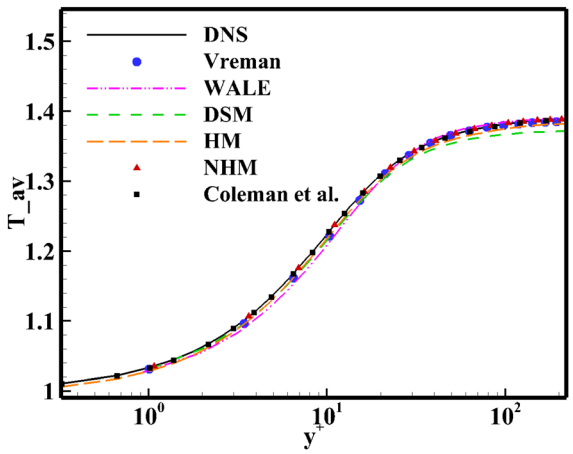

FIG. 7. Mean temperature profiles obtained from the DNS and the selected models. The results from Coleman *et al.*[38] are also listed here for comparison.

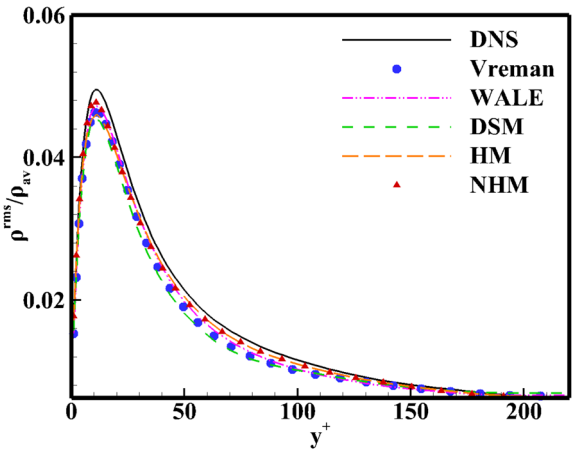

FIG. 9. Density fluctuations normalized by averaged density ρ_{av} from different SGS models and DNS.

B. Generalizing to the compressible flat-plate boundary layer

In this part, to verify the ability of the NHM in simulating other type of the compressible wall flow, we select the compressible flat-plate boundary layer as a typical testing case. Compared with the channel flow, the flat-plate boundary layer is a more complex wall-bounded flow. It is a typical flow consisting of laminar, transitional, and fully turbulent regions which are representative characters in wall-bounded flow. Therefore, the testing case can be regarded as a better case for evaluating the new SGS model in transitional and turbulent flows.

Here, the spatially developing supersonic adiabatic flat-plate boundary layer flow (at $Ma = 2.25$ and $Re = 635\,000$) is selected to test the validity of the new model. The computational domain is bounded by in-flow and out-flow boundaries, a wall boundary, a far-field boundary and two boundaries (periodic) in the spanwise direction; the computational domain has a size of $L_x \times L_y \times L_z = 6 \times 0.3 \times 0.175$. Blowing and suction disturbances[39] are imposed at the wall with an interval of x ($4.5 \leq x \leq 5.0$), and the amplitude of 0.02 is selected for this case. For convenience of comparison, we select two sets of the LES grid for testing. In Table V, we supply the grid setting of the DNS and the LES of this testing case.

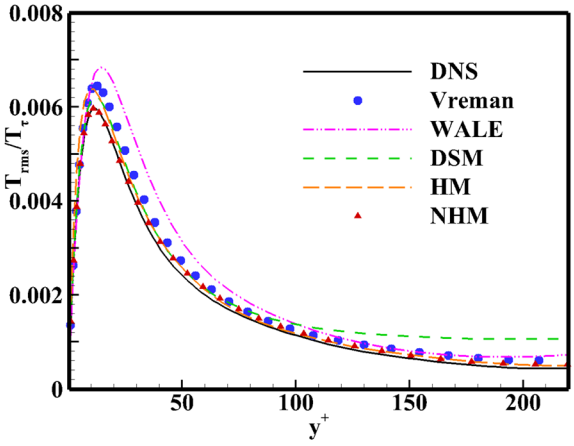

FIG. 8. Temperature fluctuations from the DNS and the selected models.

First, we show distributions of the Van Driest transformed mean streamwise velocity at $x = 8.8$ from the LESs of two sets of grids in Fig. 10, and grid-1 is fine while grid-2 is coarse. In Fig. 10(a), we can see that, under the condition of the fine grid, the velocity profile from the NHM is tightly close to the DNS which is better than other models, but the preponderance is not so evident. On the coarse grid case in Fig. 10(b), the result of the NHM still shows better behavior than other results, and the preponderance even turns more distinct.

As a key index in the compressible flat-plate boundary layer, the skin-friction coefficient distribution can accurately reflect the laminar, the transition and the turbulence, and is also a key index for testing the models. In Fig. 11, we show distributions of the skin-friction coefficients obtained from the Vreman, the WALE, the HM, the DSM, and the NHM compared with the results obtained from the DNS on two sets of grids. From the curve of the skin-friction coefficient predicted by the DNS, we can see that the occurrence of the transition is about $x = 6.3$, the transition peak is about $x = 7.2$, and the value of the peak is about 0.285. On the fine grid, all the models can supply the reasonable results, and the NHM is a little better than other models in transition peak predicting. On the coarse grid, we can easily see that the NHM has evident advantage over other model in predicting the transition process including the onset and the peak of the transition.

TABLE V. The grid setting of the DNS and the LES for the simulations in the flat-plate boundary layer.

	Grids	Δx^+	Δy_w^+	Δz^+
DNS	$10090 \times 90 \times 320$	6.02	0.58	5.47
LES1	$1500 \times 90 \times 100$	40.10	0.58	17.5
LES2	$1000 \times 90 \times 80$	60.20	0.58	21.9

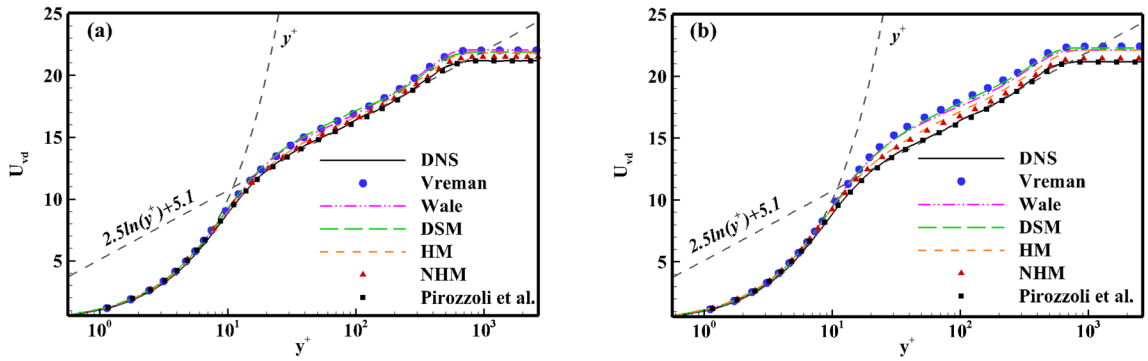

FIG. 10. The Van Driest transformed mean streamwise velocity at $x = 8.8$: (a) grid-1 and (b) grid-2. The results from Pirozzoli *et al.*[39] are also listed here for comparation.

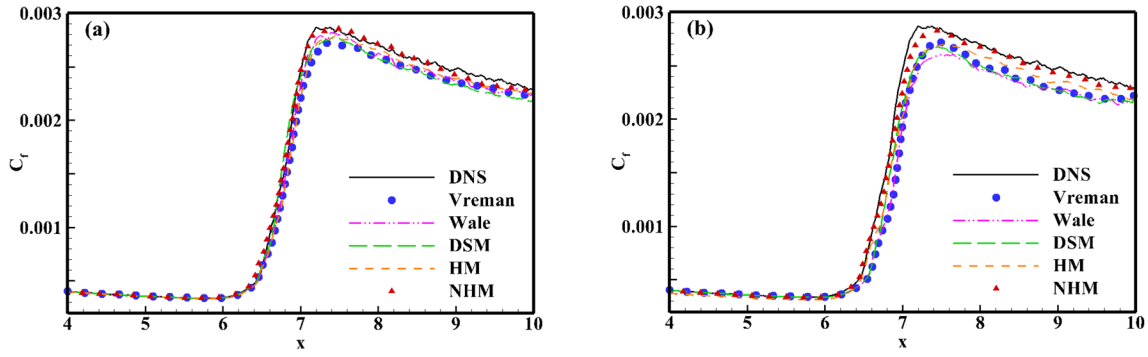

FIG. 11. The skin-friction coefficient distribution along the flat plate: (a) grid-1 and (b) grid-2.

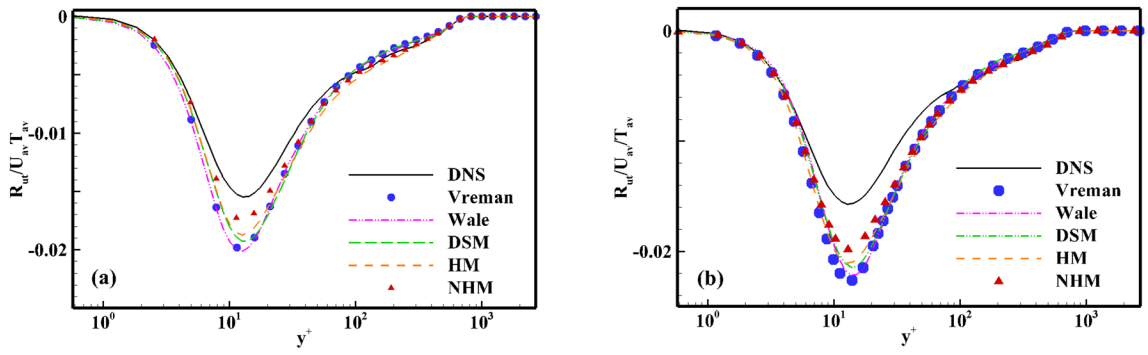

FIG. 12. The temperature–velocity correlation normalized by the product of the average temperature and the velocity along the wall-normal direction at $x = 8.8$ of the compressible flat-plate boundary layer: (a) grid-1 and (b) grid-2.

In Fig. 12, the profiles of the normalized temperature–velocity correlation along the wall-normal direction at $x = 8.8$ are shown in the two-grid resolutions. Compared with other models, the result from the NHM still has advantage, especially in the buffer-lay region. However, different from other physical quantities, the result from the NHM on the coarse grid does not show more obvious advantage over the others on the fine grid.

From the analyses of the testing case above, the NHM shows a superior ability in predicting the main physical quantities in flat-plat boundary layer, and has a good generalization to this type of the wall bounded turbulence.

V. CONCLUSION

In this paper, we propose a new rectified helical model (NHM) using the constraint of helicity flux and the method of artificial neural network (ANN) for the large eddy simulation of the compressible wall-bounded turbulent flows. Considering the helicity flux can well reflect the cascade process and the evolution of the flow structure in turbulent

flows, we use the helicity flux to constrain the old helical model for better predicting the turbulent flow. To ultimately determine the model coefficient of the simplified helicity flux, we introduce the ANN method.

First, the NHM is applied to the simulation of the compressible turbulent channel flow. Compared with other traditional eddy-viscosity SGS models, including the Vreman, the WALE, and the DSM models, the NHM can better predict typical statistical quantities than the comparing models, such as the mean profile of the streamwise velocity, the Reynolds stress, the temperature–velocity correlation, etc. Then, the NHM is also tested in a supersonic spatially developing flat-plate flow. In *a posteriori* test, the NHM could precisely predict the classic natural transition process, including the onset of the transition and the transition peak on the presupposed fine and coarse grids. Furthermore, the NHM could also provide more accurate profile of the mean velocity and the temperature–velocity correlation than other models in the cases of two sets of grids. It also proves the good generalization of the NHM for its semi-explicit character.

In summary, the new helical model suggested in this paper has been verified to be an effective method in LES of the compressible wall-bounded turbulent flows. It should be generalized to more complex wall-bounded turbulences in the future.

ACKNOWLEDGMENTS

This work was supported by the National Key Research and Development Program of China (Grant Nos. 2020YFA0711800 and 2019YFA0405302), NSFC Projects (Nos. 12072349, 12232018, 91852203, and 12202457), National Numerical Wind Tunnel Project, Science Challenge Project (Grant No. TZ2016001), Strategic Priority Research Program of Chinese Academy of Sciences (Grant No. XDC01000000), Natural Science Foundation of Gansu Provincial Science and Technology Department (Grant No. 21JR7RE171), and Natural Science Foundation of Zhejiang Guangsha Vocational and Technical University of Construction (Grant No. 2022KYQD-LWH). The authors thank the National Supercomputer Center in Tianjin (NSCC-TJ) for providing computer time.

AUTHOR DECLARATIONS

Conflict of Interest

The authors have no conflicts to disclose.

Author Contributions

Wanhai Liu: Investigation (equal); Resources (equal). **Han Qi:** Investigation (equal). **Haoyu Shi:** Data curation (equal). **Changping Yu:** Conceptualization (lead); Funding acquisition (lead). **Xinliang Li:** Data curation (lead); Funding acquisition (equal); Software (lead).

DATA AVAILABILITY

The data that support the findings of this study are available from the corresponding author upon reasonable request.

APPENDIX: HYPERPARAMETERS FOR THE ANN METHOD

In this section, we will show the predicting effects using different activation functions and neurons numbers in the ANN method.

TABLE VI. Correlation coefficient (C), relative error (Er), and ratio of root mean square value (R) of the coefficient η_Δ obtained by different activation functions and different neurons numbers for ANN3 in training cases.

ANN model	The number of neurons	$C(\eta_\Delta)$	$Er(\eta_\Delta)$	$R(\eta_\Delta)$
ANN3-tanh	10	0.893	0.152	0.891
ANN3-tanh	50	0.901	0.131	0.911
ANN3-tanh	100	0.923	0.112	0.923
ANN3-lrelu	10	0.879	0.154	0.871
ANN3-lrelu	50	0.881	0.151	0.875
ANN3-lrelu	100	0.885	0.149	0.881

TABLE VII. Correlation coefficient (C), relative error (Er), and ratio of root mean square value (R) of the coefficient η_Δ obtained by different activation functions and different neurons numbers for ANN3 in testing cases.

ANN model	The number of neurons	$C(\eta_\Delta)$	$Er(\eta_\Delta)$	$R(\eta_\Delta)$
ANN3-tanh	10	0.889	0.155	0.888
ANN3-tanh	50	0.898	0.135	0.905
ANN3-tanh	100	0.912	0.122	0.913
ANN3-lrelu	10	0.872	0.156	0.869
ANN3-lrelu	50	0.879	0.153	0.871
ANN3-lrelu	100	0.882	0.150	0.879

The activation functions are chosen as tangent function (tanh) and leaky_relu function (lrelu). The leaky_relu function can be expressed as follows:

$$lrelu(x) = \begin{cases} x, & x \geq 0, \\ \alpha x, & \text{otherwise}, \end{cases} \quad \text{where } \alpha = 0.2. \tag{A1}$$

Every case is given two hidden layers. The neuron numbers for each hidden layer are chosen as 10, 50, and 100. From Tables VI and VII, we can know that the predicting effects from tangent function and 100 neurons are best, and we can infer that the hyperparameters for the ANN method chosen in this paper are good.

REFERENCES

[1]H. K. Moffatt, "Helicity," C. R. Mec. **346**, 165–169 (2018).
[2]D. K. Lilly, "The structure, energetic and propagation of rotating convective storms. Part I. Energy exchange with the mean flow," J. Atmos. Sci. **43**, 113–125 (1986).
[3]H. K. Moffatt and A. Tsinober, "Helicity in laminar and turbulence flow," Annu. Rev. Fluid Mech. **24**, 281–312 (1992).
[4]H. Dumitrescu and V. Cardos, "Rotational effects on the boundary-layer flow in wind turbines," AIAA J. **42**, 408–411 (2004).
[5]V. Borue and S. A. Orszag, "Spectra in helical three-dimensional homogeneous isotropic turbulence," Phys. Rev. E **55**, 7005 (1997).
[6]W. T. M. Irvine, "Moreau's hydrodynamic helicity and the life of vortex knots and links," C. R. Mec. **346**, 170–174 (2018).
[7]A. Alexakis and L. Biferale, "Cascades and transitions in turbulent flows," Phys. Rep. **767–769**, 1–101 (2018).

[8]A. Brissaud, U. Frisch, J. Leorat, M. Lesieur, and A. Mazure, "Helicity cascades in fully developed isotropic turbulence," Phys. Fluids **16**, 1366–1367 (1973).
[9]R. H. Kraichnan, "Helical turbulence and absolute equilibrium," J. Fluid Mech. **59**, 745–752 (1973).
[10]J. C. Andre and M. Lesieur, "Influence of helicity on the evolution of isotropic turbulence at high Reynolds number," J. Fluid Mech. **81**, 187 (1977).
[11]P. D. Ditlevsen and P. Giuliani, "Cascades in helical turbulence," Phys. Rev. E **63**, 036304 (2001).
[12]E. B. Gledzer, "System of hydrodynamic type admitting two quadratic integrals of motion," Soviet Phys. Dokl. **18**, 216–217 (1973).
[13]Q. Chen, S. Chen, G. L. Eyink, and D. D. Holm, "Intermittency in the joint cascade of energy and helicity," Phys. Rev. Lett. **90**, 214503 (2003).
[14]S. Kurien, M. A. Taylor, and T. Matsumoto, "Cascade time scales for energy and helicity in homogeneous isotropic turbulence," Phys. Rev. E **69**, 066313 (2004).
[15]P. D. Mininni, A. Alexakis, and A. Pouquet, "Large-scale flow effects, energy transfer, and self-similarity on turbulence," Phys. Rev. E **74**, 016303 (2006).
[16]J. Baerenzung, H. Politano, and Y. Ponty, "Spectral modeling of turbulent flows and the role of helicity," Phys. Rev. E **77**, 046303 (2008).
[17]J. Smagorinsky, "General circulation experiments with the primitive equations: I. The basic experiment," Mon. Weather Rev. **91**, 99–164 (1963).
[18]J. Deardorf, "A numerical study of three-dimensional turbulent channel flow at large Reynolds numbers," J. Fluid Mech. **41**, 453–480 (1970).
[19]F. Nicoud and F. Ducros, "Subgrid-scale stress modelling based on the square of the velocity gradient tensor," Flow, Turbul. Combust. **63**, 183–200 (1999).
[20]A. W. Vreman, "An eddy-viscosity subgrid-scale model for turbulent shear flow: Algebraic theory and applications," Phys. Fluids **16**, 3670–3681 (2004).
[21]C. Yu, R. Hong, Z. Xiao, and S. Chen, "Subgrid-scale eddy viscosity model for helical turbulence," Phys. Fluids **25**, 095101 (2013).
[22]H. Zhou, X. Li, H. Qi, and C. Yu, "Subgrid-scale model for large-eddy simulation of transition and turbulence in compressible flows," Phys. Fluids **31**, 125118 (2019).
[23]J. Bardina, J. Ferziger, and W. Reynolds, "Improved subgrid-scale models for large-eddy simulation," AIAA Paper No. 80-1357, 1980.
[24]R. A. Clark, J. H. Ferziger, and W. C. Reynolds, "Evaluation of subgrid-scale models using an accurately simulated turbulent flow," J. Fluid Mech. **91**, 1–16 (1979).
[25]J. Ling, A. Kurzawski, and J. P. Templeton, "Reynolds averaged turbulence modelling using deep neural networks with embedded invariance," J. Fluid Mech. **807**, 155–166 (2016).
[26]V. Vollant, G. Balarac, and C. Corre, "Subgrid-scale scalar flux modelling based on optimal estimation theory and machine-learning procedures," J. Turbul. **18**, 854–878 (2017).
[27]C. Xie, J. Wang, H. Li, M. Wan, and S. Chen, "Artificial neural network mixed model for large eddy simulation of compressible isotropic turbulence," Phys. Fluids **31**, 085112 (2019).
[28]Z. Zhou, G. He, S. Wang, and G. Jin, "Subgrid-scale model for large-eddy simulation of isotropic turbulent flows using an artificial neural network," Comput. Fluids **195**, 104319 (2019).
[29]C. Xie, J. Wang, and E. Weinan, "Modeling subgrid-scale forces by spatial artificial neural networks in large eddy simulation of turbulence," Phys. Rev. Fluids **5**, 054606 (2020).
[30]C. Xie, Z. Yuan, and J. Wang, "Artificial neural network-based nonlinear algebraic models for large eddy simulation of turbulence," Phys. Fluids **32**, 115101 (2020).
[31]Z. Yuan, C. Xie, and J. Wang, "Deconvolutional artificial neural network models for large eddy simulation of turbulence," Phys. Fluids **32**, 115106 (2020).
[32]J. Park and H. Choi, "Toward neural-network-based large eddy simulation: Application to turbulent channel flow," J. Fluid Mech. **914**, A16 (2021).
[33]M. P. I. Martin, U. Piomelli, and G. Candler, "Subgrid-scale models for compressible large-eddy simulations," J. Theor. Comput. Fluid Dyn. **13**, 361–376 (2000).
[34]K. Bedford and W. Yeo, "Conjuctive filtering procedures in surface water flow and transport," in *Large Eddy Simulation of Complex Engineering and Geophysical Flows* (Cambridge University Press, 1993), pp. 513–539.
[35]S. Pope, *Turbulent Flows* (Cambridge University Press, 2000).
[36]R. Moser, S. Haering, and G. Yalla, "Statistical properties of subgrid-scale turbulence models," Annu. Rev. Fluid Mech. **53**, 255–286 (2021).
[37]D. P. Kingerma and J. Ba, "Adam: a method for stochastic optimization," arXiv:1412.6980 (2019).
[38]G. N. Coleman, J. Kim, and R. D. Moser, "A numerical study of turbulent supersonic isothermal-wall channel flow," J. Fluid Mech. **305**, 159–183 (1995).
[39]S. Pirozzoli, F. Grasso, and T. Gatski, "Direct numerical simulation and analysis of a spatially evolving supersonic turbulent boundary layer at m = 2.25," Phys. Fluids **16**, 530–545 (2004).